

Vegetation signature in the observed globally-integrated spectrum of Earth: Modeling the red-edge strength using simultaneous cloud data and application for extrasolar planets

P. Montañés-Rodríguez¹, E. Pallé¹ and P.R. Goode¹

Big Bear Solar Observatory, New Jersey Institute of Technology, Newark, NJ 07102, USA

pmr@bbsso.njit.edu

ABSTRACT

A series of missions will be launched over the next few decades that will be designed to detect and characterize extrasolar planets around nearby stars. These missions will search for habitable environments and signs of life (biosignatures) in planetary spectra. The vegetation’s “red edge”, an intensity bump in the Earth’s spectrum near 700 nm when sunlight is reflected from greenery, is often suggested as a tool in the search for life in terrestrial-like extrasolar planets. Here, through ground-based observations of the Earth’s spectrum, satellite observations of clouds, and an advanced atmospheric radiative transfer code, we determine the temporal evolution of the vegetation signature of Earth. We find a strong correlation between the evolution of the spectral intensity of the red edge and changes in the cloud-free vegetated area over the course of the observations. This relative increase for our single day corresponds to an apparent reflectance change of about 0.0050 ± 0.0005 , with respect to the mean albedo of 0.25 at 680 nm ($2.0 \pm 0.2\%$). The excellent agreement between models and observations motivated us to probe more deeply into the red edge detectability using real cloud observations at longer time scales. Overall, we find the evolution of the red edge signal in the globally-averaged spectra to be weak, and only attributable to vegetation changes when the real land and cloud distributions for the day are known. However, it becomes prominent under certain Sun-Earth-Moon orbital geometries, which are applicable to the search for life in extrasolar planets. Our results indicate that vegetation detection in Earth-like planets will require a considerable level of instrumental precision and will be a difficult task, but not as difficult as the normally weak earthshine signal might seem to suggest.

Subject headings: Earth’s albedo, Earthshine spectrum, astrobiology: biomarkers, red edge

1. Introduction

A spectacular astronomical revolution is on its way with the development of new scientific projects aimed at the detection and characterization of Earth-size extrasolar planets (Fridlung 2004). Among the most prominent goals of these missions will be the search for biosignatures indicating the presence of life, but life can exist in a rich variety of forms, if the Earth’s past and present is to serve us as a guide.

For most of its past history, life on Earth existed solely as unicellular microorganisms, which were able to interact with, and transform their environ-

ments. In the early Archean period (4.0-2.6 *Gyr* b.p.) for instance, methanogens were already producing CH_4 , which also has a small abiotic source, and could have generated a detectable methane-rich atmosphere (Schindler & Kasting 2000). With the advent of cyanobacteria and the subsequent rise in O_2 concentration, even larger changes in atmospheric composition took place. Thus, the remote detection of such life forms might be possible by studying the atmospheric composition of a planet (Hitchcock & Lovelock 1967).

Suppose that the necessary physical conditions for life were found on a planet, and biological fin-

gerprints are detected in its atmosphere (Hitchcock & Lovelock 1967; Selsis et al. 2002; DesMarais et al. 2002; Ford et al. 2001). Could we determine whether this life has evolved further than unicellular organisms into more complex organisms such as plants? The Earth’s vegetation has several spectral features, related to chlorophyll, that make detection of plants on Earth an easy task from space when geographical resolution is available. In particular the ‘red edge’, a sharp increase in leaf reflectance around 700 nm (Clark et al., 1993, Kiang et al., 2005), was already detected in 1993 by the Galileo mission (Sagan et al. 1993). Nowadays, vegetation leaf indices and phytoplankton blooms are routinely monitored from space.

However, when observing an extrasolar planet, all the reflected starlight and radiated emission from its surface and atmosphere will be integrated into a single spectrum. A similar kind of globally-integrated planetary spectrum for the Earth can be measured by observing the earthshine (Qiu et al. 2003; Pallé et al. 2003; Pallé et al. 2004), the light reflected by the daytime Earth onto the dark portion of the lunar surface.

Spectral measurements of the earthshine are one of the few observations one can make of disk-integrated Earth spectra. These earthshine measurements allow us to observe the Earth as it would be seen from a distant planet, i.e., with no spatial resolution. With the recent successes in the detection of exoplanets, the characterization of the spatially averaged spectral reflectance of the Earth, as provided by the earthshine technique, is becoming a keystone in the search for habitable exoplanets.

Several groups have reported in the literature analysis of their observations (Woolf et al. 2002; Arnold et al. 2002; Montañés-Rodríguez et al. 2004; Montañés-Rodríguez et al. 2005; Seager et al. 2005, Hamdani et al., 2006) or modeling (Arnold et al. 2002; Tinetti et al. 2006a) of the earthshine and tried to determine the detectability of the red edge. While some authors claimed to have detected the red edge, others are doubtful and the overall agreement between earthshine modeling and observations has been, so far, limited. The ever-present blocking cloudiness on global scales, with its high albedo, would be expected to obscure the red edge signal.

In a previous work (Montañés-Rodríguez et al., 2005), we measured with great precision the spectral albedo of the sunlit Earth, $p^*(\lambda)$, as reflected from the Moon on 2003 November 19. The earthshine-contributing area during the observations was centered sequentially over Western Africa, the Atlantic Ocean and the Amazonian rainforest. Our analysis allowed us to determine the scale of $p^*(\lambda)$, which was comparable to observations of the photometric albedo for the subsequent day, and had an average value of 0.27 ± 0.01 . In Montañés-Rodríguez et al. (2005), the good agreement between the independent photometric and spectroscopic observations of albedo confirmed the validity of applying our photometric data reduction methodology (Qiu et al., 2003; Pallé et al., 2003) to spectral data reduction.

Our analysis of earthshine data for 2003 November 19 did not show a significant vegetation signal in the Earth’s globally-integrated spectrum. We speculated that the lack of a strong red edge was due to cloud obstruction, because the Earth’s albedo is dominated by the total cloud amount and optical thickness (Pallé et al., 2004). However, we could not compare with the real cloud distribution at the time of observations because they were not yet available. Since then, global satellite observations of clouds from the International Satellite Cloud Climatology Project (ISCCP) have been released covering 2003 November 19 in the latest update, which now covers the period from July 1983 to December 2004. With these data, we have reproduced the Earth’s scene for 2003 November 19, such as it would have been viewed from a lunar perspective, and we have generated a synthetic spectral reflectance for that date and time. Finally, we have compared and contrasted our simulations and observations, and quantified the changing slope of the red edge, as Earth rotates and cloud-free vegetated areas appear and disappear from the earthshine.

2. Data

2.1. Earthshine Observations

Earthshine spectroscopic observations were taken from Palomar Observatory with the 60-inch telescope (P60”).

A single order, long slit spectrograph with an entrance slit of 1.32” x 6’ on the sky was selected;

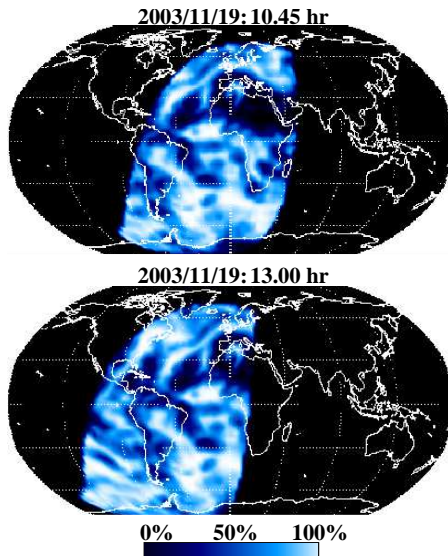


Fig. 1.— Map of the earthshine-contributing area during the observations on 2003 November 19. Top: 10:45 UT; Bottom: 13:00 UT. Although the earthshine contributing area and solar and lunar cosines have been calculated for the exact times of our observations, the time resolution of the ISCCP data is 3 hours. Thus, the cloud data represented in the two maps correspond to 9:00-12:00 UT and 12:00-15:00 UT ISCCP data bins. Still, one can note how little the cloud cover did change during the night. In particular, compare the clouds over South America in the upper and lower panels.

for comparison, the mean lunar apparent diameter during the time of observations was $32.24'$. We covered the spectral region between 460 nm and 950 nm with a resolution of 7.1 \AA at 700 nm. We took alternate exposures of the bright and dark side of the Moon, the dark side exposures including a large portion of the background sky, with signal to noise ratios of 500 and 30 respectively. The ratio between the signal of the dark side and the immediately surrounding background sky was of the order of 2.5. The ratio between dark and bright side spectra gives us, after accounting for several geometric corrections, the Earth's albedo as a function of wavelength. Detailed data acquisition techniques and data reduction for the earthshine spectra presented here can be found in Montañés-Rodríguez et al. (2005).

2.2. Satellite Cloud data

The ISCCP dataset provides continuous global coverage of cloud amount and radiative properties, from the combined observations of several inter-calibrated geosynchronous and polar satellites. In the ISCCP dataset, total cloudiness is determined using both visible and infrared radiances, whereas the separation into low, mid and high level cloud types is determined using infrared radiances only. The data are given for $280 \times 280 \text{ km}^2$ cells with the cloud fraction in each cell determined by dividing the number of cloudy pixels by the total number of pixels per cell. All ISCCP data products are available at the ISCCP Central Archive¹, and a detailed description of the whole dataset can be found in Rossow et al. (1996).

In Figure 1, we have used the ISCCP data to determine the evolution of the cloud-geography pattern for the date (2003 November 19) and times (from 10:28:12.0 to 13:04:47.9 UT) of our observations. Note that on the timescale of our observations (~ 3 hours), the variability in the large-scale cloud patterns is very small, and the clouds can be considered fixed with respect to the geography. We have calculated the percentages of cloud-covered areas and cloud-free oceans, land, ice and vegetated areas over the entire earthshine-contributing region during observations (given in Table 1). The cloud percentage at each grid point of the Earth has been further subdivided into low, mid and high level clouds according to the ISCCP IR radiance classifications. To simulate the Sun-Earth-Moon earthshine geometry for the date/times and thus allow a direct comparison of the model and observations, these global percentages have been weighted by the solar and lunar cosines at each point of the Earth.

3. Radiative transfer simulations of the earthshine

The synthetic generation of earthshine spectra has been carried out using the state-of-the-art atmospheric code FUTBOLIN. FUTBOLIN (Full Transfer By Optimized LINE-by-line methods) is a multi-level, multiple scattering radiative transfer model for the calculation of line-by-line atmospheric emission/transmission spec-

¹<http://isccp.giss.nasa.gov>

Table 1: Composition (in percentages) of the Earth scene for 2003 November 19 in the earthshine field of view for our observations. Clouds refer to the total cloud amount including low, middle and high altitude clouds. Land percentages includes shrub, tundra and desert regions free of clouds. Vegetation refers to cloud-free vegetated areas. The total ice/snow area during observations was always less than 0.1%.

Time (UT)	clouds	oceans	land	vegetation
10:00	58.59	16.37	9.03	15.90
10:30	59.34	17.33	7.90	15.34
11:00	59.90	18.52	6.76	14.75
11:30	60.27	19.73	5.70	14.23
12:00	60.46	20.72	4.75	14.01
12:30	60.42	21.36	3.99	14.16
13:00	60.30	21.73	3.36	14.56

tra in planetary atmospheres (Martín-Torres et al. 2005; Kratz et al. 2005). It can generate high-resolution synthetic spectra in the 0.3-1000 micron spectral range, using as its principle inputs the atmospheric profiles from a 3-D global circulation model (García et al. 1992), the spectral albedos from the ASTER (Advanced Spaceborne Thermal Emission and Reflection Radiometer) and TES (Thermal Emission Spectrometer) libraries², and the spectroscopic data from the HITRAN2K (High-resolution TRANsmission molecular absorption) database (Rothman et al. 2003). Solar irradiance data in the 490-940 nm spectral region is taken from the AIRS (Atmospheric InfraRed Sounder) database.

FUTBOLIN has been previously compared to other atmospheric models, such as LBRM, LINEPAK, GENLN2 and MRTA, with a remarkably good agreement in the results, with differences being of the order of 0.5% (Kratz et al. 2005). It has been also successfully applied to the analysis of terrestrial and planetary spectra of Venus and Titan (Martín-Torres et al. 2003a, and 2003b).

For the simulations shown in this paper, the Earth is treated in 1-D, as a single cell, for which the averaged atmospheric, surface and cloud properties are given. The atmosphere for the night was

described through a standard atmospheric composition, temperature and pressure profiles (García et al. 1992). We have used Voigt profiles as the lineshapes of atmospheric gases through the atmosphere, and a number of physical phenomena like multiple scattering, continuum absorption by water vapor, CO_2 , N_2 and O_2 , and line mixing in the CO_2 bands. The spectra have been computed with a $0.0005cm^{-1}$ resolution and have been degraded to the observation's instrumental resolution.

Using global cloud maps from ISCCP, we calculated a global mean percentage of clouds and surface types, weighted by the solar and lunar cosines. These percentages were used to average the computed spectra for each type of surface considered into a global mean. Clouds were separated into the three ISCCP IR cloud categories (low, mid and high) have been modeled as Strato-cumulus, Alto-stratus and Cirrus, respectively (Manabe & Strickler 1964). Cloud spectral calculation include multiple scattering (Mie scattering) and are parameterized using bi-directional reflectance functions (BDRFs) for each cloud type. The mean solar and lunar cosine angles over the earthshine-contributing area, were defined as the incident and reflecting angles respectively.

The resultant synthetic spectrum for 2003 November 19, based on the mean of the percentages given in Table 1, is compared to the average of all observed spectra in Figure 2. As can be seen in the figure, there is an excellent agreement over almost the entire spectral range covered; the major discrepancy is in the depth of the absorp-

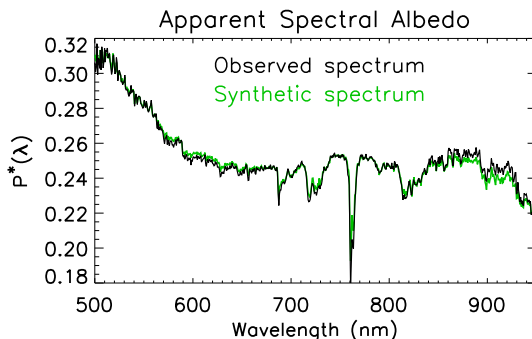


Fig. 2.— Averaged observed and synthetic Earth's apparent spectral albedo for 2003 November 19, for the entire spectral range of our observations.

²<http://speclib.jpl.nasa.gov> ; <http://tes.la.asu.edu>

tion bands and derives from the complexity of the treatment of the multiple scattering in the simulations. This agreement represents a real improvement over earlier efforts to fit earthshine observations with models, and gives us strong confidence in our observational data.

4. Red edge evolution during observations

In Figure 3, the eight earthshine spectra taken on 2003 November 19 are plotted. To determine the intensity of the red edge, we calculated the slope of a straight line connecting the red edge to the nearby spectral continuum. This is the dashed line, in each of the eight panels of Figure 3, connecting two selected spectral regions (marked as shadowed strips also in Figure 3). The choice of bands is made to avoid the atmospheric absorption bands of O₂-B (centered at 690 nm), H₂O (centered at 720 nm) and O₂-A (centered at 760 nm). The regions were fixed to the ranges 678–682 nm and 740–750 nm and contained 6 and 14 data points, respectively. We determined the percentage increases of the spectra between 680 and 740 nm, by applying a linear fit to all data points contained within the two selected regions, for each of the eight observed spectra and for a set of seven synthetic spectra. The slope of the dashed line was relatively insensitive to the choice of the narrow band near 680 nm in Figure 3. That is, the relative slopes of the red edge were about the same whether the band near 680 nm was made broader or moved to a slightly different wavelength. The synthetic spectra were generated with a time step of 30 minutes, using the percentages given in Table 1, and also distinguishing between low, middle and high clouds and a variety of land surfaces (shrubs, tundra and deserts).

The percent increase in reflectance for the observed spectra varied between $2.77 \pm 0.22\%$ and $2.23 \pm 0.16\%$, and are indicated in Figure 3. In the case of the synthetic spectra, the slopes were consistent with, but more subtle than the variations in the observational data. In detail, the percent increases in the models varied between $0.30 \pm 0.01\%$ and $0.07 \pm 0.01\%$. We attribute the more subtle model variations to the difficulty in the treatment of the scattering. In particular, the continuum near 680 nm is inside a weak O₃ band, and we anticipate that this part of the spectrum would

drop with an improved treatment of the multiple scattering, thus improving the agreement with the observed slopes in Figure 3. The rise in the observed spectra was in general more sensitive to the width of the spectral regions selected for the linear fit, than it was in the synthetic spectra due to the noise in the observational data.

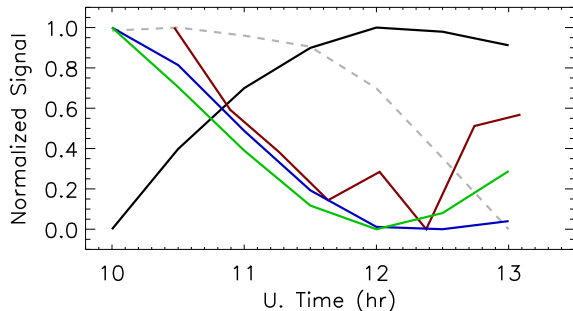


Fig. 4.— Evolution of different signals during observations: 680–740 nm rise for the models (blue). 680–740 nm rise for the observations (red). Total cloud-free vegetated areas (green). Total cloud amount (solid gray). Low-cloud amount (dotted gray).

We emphasize that for both models and observations, the slopes varied according to the change in the percentage of cloud-free vegetated areas, and in opposition (anti-correlation) to the change in total cloud amount. The normalized evolution of the cloud-free vegetated areas, cloud coverage and the red-edge rises are shown in Figure 4. We calculated the correlation between the decline of normalized cloud-free areas of vegetation and the red-edge decline for models and observations over the course of the observations. To correlate the areas of vegetation with the rise of the red edge in the observations, the former were interpolated to the times of our observations. The correlations were 0.95 for the models and 0.91 for the observations, respectively. In Figure 5 the observed red edge slope in our earthshine measurements is plotted against the cloud-free vegetated area measured from satellite data. The significant correlation shown in the plot is probably the first unambiguous detection of vegetation on Earth on global scales.

However, we note that vegetation is not the

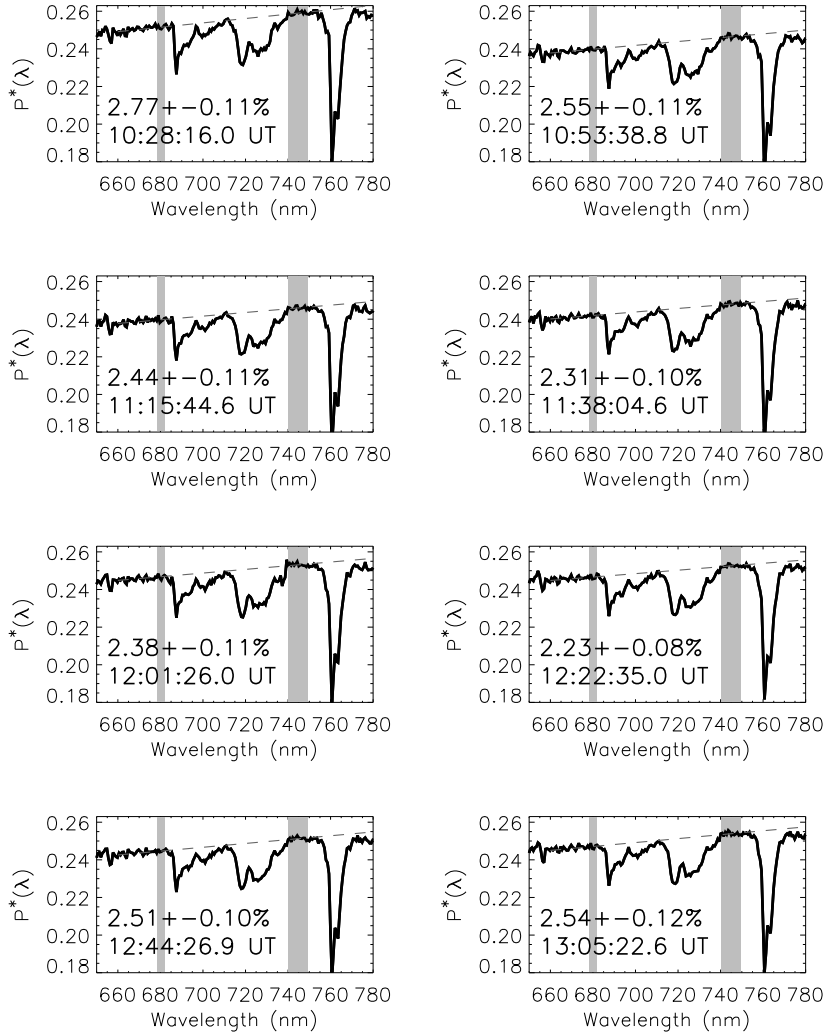


Fig. 3.— Evolution of the earthshine spectrum during the observations on 2003 November 19. Shaded strips in each panel indicate the two sectors used to determine the red-edge slope. The percentage rise between 680 and 740 nm, and the time of observation (UT) are also indicated. The narrow strip in each panel is a continuum region that doesn't show much variation. Various spectral positions and widths of the narrow band of continuum were tried with similar results for the relative increase of the red edge bump. The dashed line in each panel connecting the broad and narrow strips indicates the slope from which the change in intensity in the red edge is determined.

only possible source of the bump in the 680–740 nm region, clouds effects may also cause it because varying the quantity or type of clouds into the scenery will produce differential changes in albedo along the spectra (Tinetti et al., 2006a). In particular, low clouds are bright at these wavelengths and add to the red-edge slope, while other relatively darker surface components, such as oceans, non-vegetated land areas and snow or ice, cause a decline in the red edge intensity (Tinetti et al., 2006a). Thus, the quantification of the red-edge slope does not alone provide a direct vegetation strength index in globally-integrated measurements. However, we find no significant correlation between the low cloud amount and the red edge variability during our observations (see Figure 4).

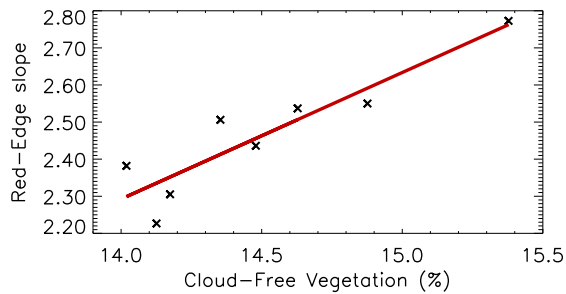


Fig. 5.— Scatter plot of the projected cloud-free vegetated areas measured from satellite, and the strength of the red edge slope in the earthshine observations.

To eliminate the possibility that the decrease found in the red-edge slope was due to changes in cloud percentage in the evolving field of view during the observations, we carried out a final test. New models were calculated for the times shown in Table 1. All of them with a fixed cloud amount in the field of view, the same found at the beginning of our observations. The same percentages shown in Table 1 were used for the remaining components of the scene, except for the oceans. The percentage of total ocean area was slightly modified to ensure that the total of all components add to 100% and compensate for the fixed cloud percentages. The correlation found between the red-edge rises for these new models and the evolution of the cloud-free vegetated areas was still 0.93, indicating that

the cloud-free vegetated areas, and not clouds, are responsible of the red-edge evolution seen in our observations.

Thus, we conclude that the observed evolution of the red edge signal during our observations is attributable to the change in cloud-free vegetated areas contributing to the earthshine at each time. However, this attribution is only possible because the real land and cloud distributions for the day are known. Without these data, which will not be available in the case of an extrasolar planet observation, we could not conclude that we are detecting the red edge (Montañés-Rodríguez et al, 2005).

5. Evolution of the red edge at longer time scales

The excellent agreement between our observations and the models, motivated us to study the evolution of the vegetation signature in the Earth’s spectra on larger time scales, for which observations are not available but global cloud data is.

Here we have modeled the temporal evolution of the vegetation’s signal strength in the earthshine using cloud cover maps from the ISCCP dataset. Considering the relative positions of the Sun-Earth-Moon system, the percentage of the Earth’s surface that is free of clouds and visible from the Moon is computed for each day at each point of a grid surface. This percentage is subdivided into percentages corresponding to oceans, snow/ice, vegetated areas, shrubs, deserts and tundra. Similarly the percentages of low, mid and high-altitude clouds are computed. These percentages are then combined for the whole earthshine-contributing area, weighted by the solar and lunar cosines at each grid point to account for the true earthshine signal. For comparison, we have also calculated these percentages in the direction of the Sun (retroreflection) from where the whole sunlit half of the Earth’s surface is always visible. Our projected percentages are used as input for FUTBOLIN, which calculates the spectral features of such a projection.

The top panel in Figure 6 shows the 1-hour resolution cloud-free vegetated area contributing to the earthshine for year 2003. Note that this contribution is in earthshine-contributing surface percentage (weighted by the solar and lunar cosines

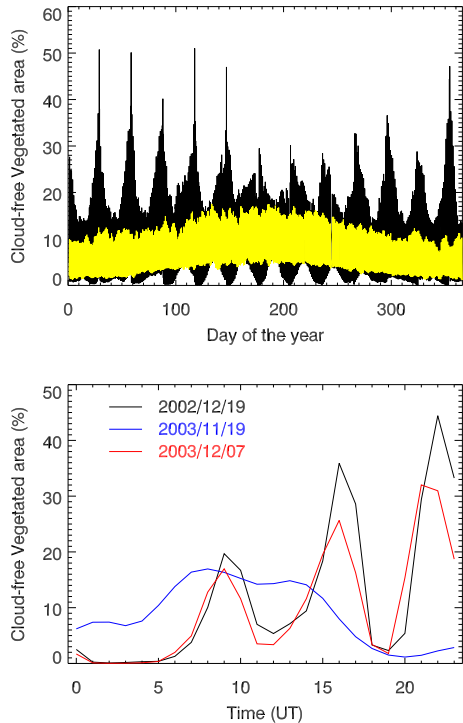


Fig. 6.— Top panel: Percentage of the total earthshine-contributing area that is simultaneously cloud-free and covered by vegetation (black) though the year 2003. The percentages are weighted by the solar and lunar cosines and calculated with a 1-hour time resolution. In yellow are the percentages of total sunlit area which are simultaneously cloud-free and covered by vegetation. Note the largest excursion of the black curve due to the Moon’s orbital cycle (glint scattering of sunlight from a heavily vegetated areas of a crescent Earth) . Bottom panel: Top panel data for three particular days, but showing the part of the earthshine heading toward the Moon. Blue: 2003 November 19 a day with an average vegetation percentage contribution. Black: 2002 December 19 a day with extreme vegetation percentage (and with an earthshine-contributing area near zero). Red: 2003 December 7, a day with a large, detectable vegetation percentage (30%) and an earthshine-contributing area 10% of the maximum (1/2 the total of the Earth’s surface). The three peaks in the red and black curves correspond to times when heavily vegetated areas rotate into view (in this case: Asia, Africa and South America from left to right).

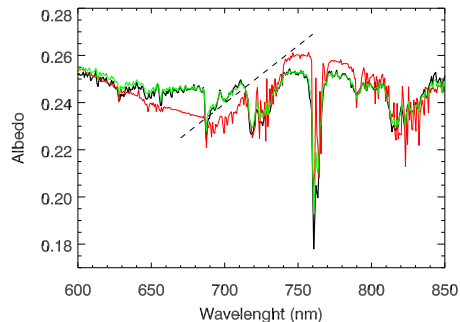


Fig. 7.— Black: Earthshine spectral albedo measured from Palomar Mountain observatory on 19 November 2003. Blue: Modeled spectral albedo using the FUTBOLIN code and the weighted percentage coverage for the same date and time of the observations (10:00 UT). Note the excellent agreement between model and observations. Red: Modeled spectral albedo for 2003 December 7 at 21:00 UT. For 2003 December 7, a strong vegetation red edge (starting around 700 nm) is visible. This is due to the large relative percentage of cloud-free vegetated area in the Earth region contributing to the earthshine.

at each point of the Earth), but the real contribution to the earthshine spectrum needs to be further weighted by the wavelength-dependent albedo of each Earth scene component (clouds, deserts, etc...). For most of the year, the vegetation’s contribution is close to that during 2003 November 19 for which ground-based earthshine observations are available. However, the contribution peaks at certain times, when the Earth as seen from the Moon is a thin crescent, and the earthshine-contributing area is small. This is illustrated in the lower panel of Figure 6, where the daily cycle of the vegetation visibility from the Moon is plotted for three different days. This daily cycle depends on both the lunar phase and the specific cloud distribution for that day. Note the large vegetation contribution at certain times of the day 2002 December 19 reaching almost 50%. At these times the red edge would be easily detectable in the global spectrum, but the Earth’s crescent is so small that the flux in the observer’s direction (in our case, the Moon) is close to zero.

Thus, to detect vegetation one needs to find a

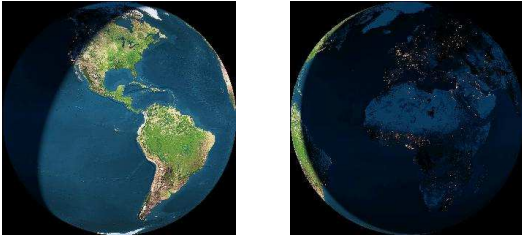


Fig. 8.— The earthshine-contributing area as viewed from the Moon. Left: For 2003 November 19 at 10:00 UT (black data and green model in Figure 7), with lunar phase $+117^\circ$. Right: for 2003 December 7 at 21:00 UT (red model in Figure 7), with lunar phase -25° . In the left panel, large vegetated and un-vegetated areas are visible, while in the right, the Earth is seen as a thin crescent and a large proportion of the sunlit area is covered by vegetation. Note that both images are very misleading, because the cloud cover is missing, which will alter the scenery. The observations studied in this paper for 2003 November 19 show only a very weak red edge despite the Amazonian rainforest being in view. This is because in the left panel the total cloud-free vegetated area, projected in the Moon’s direction, is 15% of the total sunlit area, while in the right panel it is 48%.

compromise between the Earth’s scattering area, given by the projection of the total sunlit planetary surface in the observer’s direction, and the maximum percentage of cloud-free vegetated area on that projection. Analysis of 2003 cloud data indicates that during 70 hours (almost 3 full days), the scattering cross-section of the Earth was between 5-15% of the maximum possible area (half of the planet), while cloud-free vegetated areas were higher than 25% of the contributing area. Most of these dates occurred near, but not during, the full Moon. Empirically, we have determined that a 25-30%, or upward, cloud-free vegetated area is enough to enable an unambiguous red edge detection, but the particular detection threshold for a given day will vary with cloud and surface type distributions in the remaining area.

The earthshine spectrum for 2003 November 19 as observed from Palomar Observatory (Montañés-Rodríguez et al. 2005a) is plotted in Figure 7. Also plotted is the modeled earthshine spectrum using the ISCCP cloud distribution for

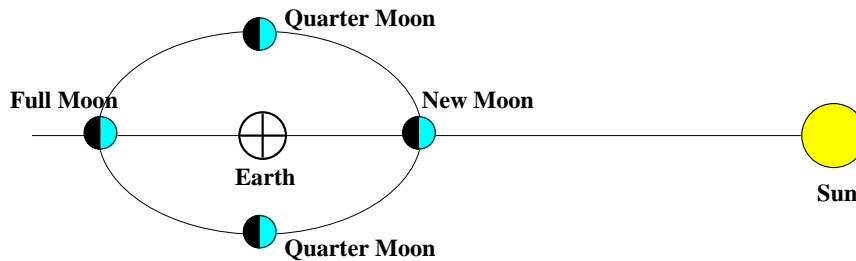
the same date and times. As shown in Section 3, model and observations agree well in their overall shape and spectral features, but the vegetation red edge is weak/missing in both because the signal is blocked by the cloud cover. Also plotted is our modeled spectrum using the cloud percentages for 2003 December 7 at 21:00 UT, a time when satellite data indicate a cloud-free vegetated area close to 30% (Figure 6). The model shows that the vegetation’s red edge is easily detectable at such times. Unfortunately observations for dates like 2003 December 7 are impossible from ground-based observatories, because at these times the Moon is almost full and the earthshine is swamped by atmospheric light scattering. However, our results indicate that if the reflected earthshine spectrum in the dark side of the Moon were to be measured from satellite platforms at lunar phases close to full Moon ($7^\circ - 27^\circ$), a clear vegetation signal would be detected.

6. The Earthshine-Exoplanets connection

The earthshine case, i.e., the Moon’s monthly evolving view of the Earth, has a counterpart in the annual cycle of an extrasolar planet around its parent star. Viewed from the distance, if our observational line of sight is reasonably close to the planet’s ecliptic plane, the planet will offer waning and waxing phases with its translation movement. This is illustrated in Figure 9

There is a certain degree of uncertainty in applying our knowledge based on Earth standards to extrasolar planets, but taking the Earth’s example, in order to sustain plant life, it is likely that the planet needs substantial amounts of liquid water, i.e. oceans, covering relatively large areas of its surface. It is also likely that a significant amount of water vapor (clouds) is present, and even tectonic activity (continents), to ensure climate stability, may be necessary to harbor life (Kasting et al. 1984). Ignoring the phytoplankton contribution, which has a lower albedo than leaves due to its water cover (Gower et al. 2004), vegetation will be limited to land areas. Thus, as the planet orbits around its star and rotates, the vegetation signal should become more dominant at certain periods of time as the planet approaches its orbital point closer to the observer. Based on our above calculations, the vegetation’s red edge

Earth view of the Moon



Earth view of an extrasolar star–planet system

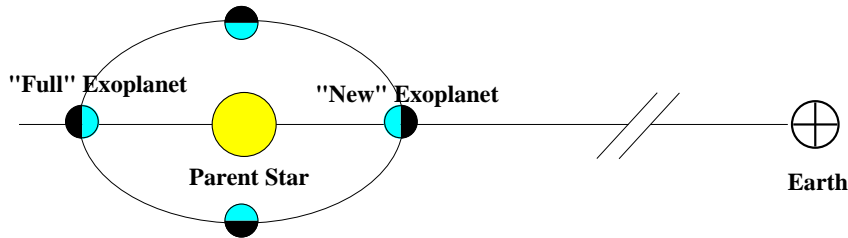


Fig. 9.— A not-to-scale cartoon illustrating the similarity of observing the earthshine at different lunar phases and observing an extrasolar planet as it orbits its star. Top: As the Moon rotates around the Earth, it waxes and wanes from full Moon to new Moon. The phases of the Earth and Moon are supplementary. Thus, at new Moon, the area contributing to the earthshine is half of the planet. In other words, an observer on the Moon would see a “full” Earth. Similarly at full Moon, the earthshine contributing area is nearly zero. Bottom: As the exoplanet revolves around its star, a Earth-bound observer would see the planet’s scattering area waning and waxing. For simplicity, in the cartoon the angle between the observer’s line of sight and the planet’s ecliptic plane is set to be zero, but the exoplanet’s observable phase range from Earth will vary greatly depending on this angle. Vegetation detection on the exoplanet will become easier near “new” (from the point of view of the Earth) exoplanet phases, during glint scattering from heavily vegetated area(s). However, there is a trade-off here because very close to “new”, it will be even more difficult to distinguish the exoplanet from its star.

could be detectable in an earth-like planet during 11% of the planet’s orbital period (40 days a year for Earth), during an undetermined number of hours each day (typically 2-3 hours for Earth).

However, despite the advantageous vegetation signal, there are some disadvantages to the observations of extrasolar planets at such times of their orbits. When the planet is in the desired phase range, typically only about 10% of the planet’s sunlit surface is visible to the observer, which means that the planet’s signal will be faintest compared to its parent star. Considering the Earth as roughly Lambertian (Qiu et al. 2003), the instrumental detection power would need to increase between one and two orders of magnitude, in order to retrieve the same spectral quality than for the same planet viewed at phase 0° (‘full’ planet).

Of course, for Earth-like extrasolar planets, the issue has the additional complication of the strong signal from the star, which would be more effectively nulled the greater the angular separation of the planet and its star. If the extrasolar planet is angularly close to the star, it is difficult to null-out the star (or otherwise remove its spectral signature) without nulling out the planet. This angular distance decreases as the planet reaches toward “new”, depending on the tilt angle between the observer and the exoplanet’s ecliptic plane. A small increase in this tilt angle will also increase the angular separation between the exoplanet and the parent star, but too much of an increase will reduce the observable phase range of the exoplanet and eliminate those we are interested in. Thus, there is a trade-off here to obtain observations at an angular separation large enough to preserve the planet’s signal, but small enough to benefit from a rough geographical resolution that allows the detection of vegetation. It is probable that none of the missions currently on design phase will be able to retrieve this measurements.

Through this manuscript, we have discussed plant detection in extrasolar planets based on chlorophyll pigment properties typical of Earth plants, but the universality of chlorophyll is still an open question (Wolstencroft & Raven 2002). The same detection criteria, however, might apply for different pigmentation or equivalent red edge signatures, characteristic of the plant type that might exist in an extrasolar planet, provided that these features do not coincide with spectral

regions with strong atmospheric absorption. Segura et al. (2005) and Tinetti et al. (2006b) have recently published studies about the possibility of an “equivalent” vegetation red edge on planets around M stars.

7. Conclusions

In our analysis of earthshine observations from 19 November 2003, we find an increase in spectral reflectance, between 680 and 740 *nm* of the order of 0.005, which is highly correlated with the evolution of the cloud-free vegetated areas contributing to the earthshine. The good agreement between the evolution of the red-edge slope for both models and observations with the total cloud-free vegetated areas, might not be enough to confirm the detection of vegetation in globally-integrated Earth’s spectra. However, the 0.93 correlation between the fixed cloud contribution models and the evolution of the cloud-free vegetated area confirms it. Nevertheless, the change in reflectance in this spectral region can only be related to vegetation by analyzing the real distribution of land, oceans and clouds during observations.

It is possible that an Earth-size extrasolar planet may have a drastically different cloud cover system that yields a stronger globally integrated vegetation signal. However, for an Earth-like planet, the impossibility of knowing beforehand the cloud distribution contributing to the planetary reflectance would seem to make it very difficult to unambiguously detect the red edge signature of vegetation.

We have also made use of the earthshine models and long-term terrestrial cloud data to simulate the evolution of the red edge signature with time, and we make the analogy between earthshine and extrasolar planets; we demonstrate that there are days on Earth with strong red edge signals, unlike the day discussed here, and that, under certain orbital conditions, for a terrestrial-like planet there are optimal times for detecting the red edge.

In summary, we have shown that the detection of vegetation on Earth using globally-integrated spectral measurements is generally very difficult, but becomes feasible under the appropriate geometrical conditions. Similarly, for an Earth-like extrasolar planet, the vegetation signature will become detectable during certain times of its orbit.

The excellent agreement of our earthshine observations with modeled spectra of the Earth using real cloud distributions for the same dates and times, gives us a strong confidence in our results, which provide a reference for future space missions aiming at the detection of such vegetation signatures in extrasolar planets. In this case, observations will require extremely sensitive instrumentation, still outside the scope of current design-phase missions, but acquiring the necessary technology seems to be only a matter of time.

This research was supported by the 2002 Ernest F. Fullam Award of the Dudley Observatory and by a grant from NASA (NASA-NNG04GN09G).

REFERENCES

- Arnold, L., S. Gillet, O. Lardiere, P. Riaud, and J. Schneider, 2002. *Astronomy & Astrophysics*, 392, 231-237
- Clark, R.N., Swayze, G.A., Gallagher, A.J., King, T.V.V. & Calvin, W.M. 1993, The U.S. Geological Survey, Digital Spectral Library: Version 1: 0.2 to 3 microns. <http://speclab.cr.usgs.gov>
- DesMarais, D., et al., 2002. *Astrobiology*, 2, 2, 153-181
- Ford, E.B., S. Seager, and E.L. Turner, 2001. *Nature*, 421, 885-887
- Fridlung, M.C., 2004. *Proceedings of SPIE*, 5491
- García, R., F. Stordal, S. Solomon, and J.T. Kiehl, 1992. *J. Geophys. Res.*, (D12), 12967-12991
- Gower, J., S. King, G. Borstad, and L. Brown, 2004. *Gayana (Concepc.)*, 68, 246-251, ISSN 0717-6538
- Hamdani, S. et al., 2006. [arXiv:astro-ph/0510611](http://arxiv.org/abs/astro-ph/0510611) (submitted).
- Hitchcock, D.R., and J.E. Lovelock, 1967. *Icarus*, 7, 149-159
- Kasting, J.F., J.B. Pollack, and T.P. Ackerman, 1984. *Icarus*, 57, 335-355
- Kiang, N. Y., A. Segura, V. Meadows and M. Cohen, 2005. *Astrobiology* 5(2): 209.
- Kratz, D.P., M.G. Mlynczak, C.J. Mertens, H. Brindley, L.L. Gordley, J. Martín-Torres, F.M. Miskolczi, and D.D. Turner, 2005. *J. of Quantitative Spectroscopy & Radiative Transfer*, 90, 3-4, 323-341
- Manabe, S., and R.F. Strickler, 1964. *Journal of Atmospheric Sciences*, 21, 4, 361-385
- Martín-Torres, J.F., et al., 2003a. EGS - AGU - EUG Joint Assembly, Abstract num. EAE03-A-07023
- Martín-Torres, J.F., et al., 2003b. EGS - AGU - EUG Joint Assembly, Abstract num. EAE03-A-07735.
- Martín-Torres, F.J., et al. 2005, *J. of Quantitative Spectroscopy & Radiative Transfer* (submitted).
- Montañés-Rodríguez, P., et al., 2004. *Advances in Space Research*, 34, 293
- Montañés-Rodríguez, P., E. Palle, P.R. Goode, J. Hickey, and S.E. Koonin, 2005. *The Astrophysical Journal*, 629, 1175-1182
- Pallé, E., et al., 2003. *J. Geophys. Res.*, 108(D22), 4710, doi:10.1029/2003JD003611
- Pallé, E., P.R. Goode, P. Montañés-Rodríguez, and S.E. Koonin, 2004. *Science*, 304, 1299-1301
- Qiu, J., et al., 2003. *J. Geophys. Res.*, 108(D22), 4709, doi:10.1029/2003JD003610
- Rossow, W.B., A.W. Walker, D.E. Beusichel, and M.D. Roiter, 1996. *International Satellite Cloud Climatology Project (ISCCP) Documentation of New Cloud Datasets*. WMO/TD-No. 737, World Meteorological Organization, 115 pp.
- Rothman, L.S., et al., 2003. *J. of Quantitative Spectroscopy & Radiative Transfer*, 82, 1-4, 5-44
- Sagan, C., W.R. Thompson, R. Carlson, D. Gurnett, and C. Hord, 1993. *Nature*, 365, 715-721
- Schindler, T.L., and J.F. Kasting, 2000. *Icarus*, 145, 262-271
- Seager, S., E.L. Turner, J. Schafer, and E.B. Ford, 2005. *Astrobiology*, 5(3), 372-390

Segura, A., J. Kasting, V. Meadows, M. Cohen, J. Scalo, D. Crisp, R. A. H. Butler and G. Tinetti, 2005. *Astrobiology* 5(2): 204

Selsis, F., D. Despois, and J.P. Parisot, 2002. *Astronomy & Astrophysics*, 388, 985-1003

Tinetti, G., et al. 2006a. *Astrobiology*, Feb 2006, Vol. 6, No. 1: 34-47.

Tinetti, G., et al. 2006b, AbSciCon 2006, Abstract #352.

Wolstencroft, R.D., and J.A. Raven, 2002. *Icarus*, 157, 535-548

Woolf, N.J., P.S. Smith, W.A. Traub and K.W. Jucks, 2002. *The Astrophysical Journal*, 574, 430-433